Focal mechanism and slip history of the 2011 M_w 9.1 off the Pacific coast of Tohoku Earthquake, constrained with teleseismic body and surface waves

Guangfu Shao[1,2], Xiangyu Li[1,2], Chen Ji[1,2], and Takahiro Maeda[3]

[1]*Department of Earth Science, University of California, Santa Barbara, Santa Barbara, CA 93106, USA*
[2]*Earth Research Institute, University of California, Santa Barbara, Santa Barbara, CA 93106, USA*
[3]*National Research Institute for Earth Science and Disaster Prevention, Tsukuba 305-0006, Japan*

(Received April 12, 2011; Revised June 16, 2011; Accepted June 17, 2011; Online published September 27, 2011)

Focal mechanism and slip history of the 2011 M_w 9.1 off the Pacific coast of Tohoku, Japan earthquake were derived rapidly from teleseismic body and surface waves. Multiple double couples (MDC) analysis was first conducted using 1-hour long period seismic waves, yielding a single double couple with a seismic moment of 5.06×10^{22} N m, whose low angle nodal plane orients 199° and dips 10° west. Spatiotemporal rupture history was then constrained using both broadband body waves and long period seismic waves. The solution was updated twice in three days. Our preferred model, which based on the MDC fault plane, local JMA hypocenter and calibrated alignments of body and surface waves, revealed a complex rupture process. The rupture initiated slowly at a depth of 23 km. It first propagated in downdip and bilaterally directions along the subduction interface for 45 s and then broke a 80 km by 250 km near trench asperity in the up-dip direction and produced up to 60 m slip. The fault plane below the hypocenter had two more subevents, occurring in 70–95 s and 110–160 s, respectively. The total seismic moment was 5.8×10^{22} N m. The abnormal high slip near the trench suggests a recurrence interval larger than 500 yr.

Key words: Multiple double couples analysis, finite fault rupture, near trench asperity.

1. Introduction

At local time 2:46 pm March 11, 2011, a great earthquake shook the off shore of Tohoku region. Its epicenter located by Japan Meteorological Agency (JMA) is (38.10°N, 142.86°E) at a depth of 24 km. The fatality due to the catastrophic tsunami waves excited by this event is about 15,000 and 8,000 people are still listed as missing. The large tsunami damaged the Fukushima nuclear power plant, which leads to serious nuclear pollutions. Here, we study this earthquake using the continuous broadband seismic data automatically fetched from Incorporated Research Institute of Seismology (IRIS) data manage center.

For a shallow focus source, the intervals between *P* and *PP*, and *S* and *SS* phases in teleseismic distances (for $30^\circ < \Delta < 90^\circ$) are usually free of significant teleseismic phases. These clear windows have then been widely used to estimate the rupture processes of global large earthquakes (e.g., Kikuchi and Kanamori, 1991; Ji *et al*., 2004). However, the drawback of this approach is also well known. The inverted results based only on this dataset are insensitive to the smooth rupture, particularly for large subduction earthquakes (Beck and Ruff, 1987; Kikuchi and Fukao, 1987; Ekström, 1989). Mendoza *et al*. (1994) introduced the concept of combined the body waves and long period surface waves together to the finite fault source study. In view of its advantage during the study of the 2004 Sumatra-Andaman island earthquake (Ammon *et al*., 2005), we had developed a quick algorithm to routinely monitor global large earthquakes by joint inverting body and surface waves. Such a joint inversion allows us to constrain the general patterns of a spatiotemporal rupture process with long period surface waves and then superpose fine structures to match broadband body waves. The uniqueness of our approach is the use of both long period Rayleigh and Love waves. They have different sensitivities to the depth of the source. Combining them together significantly improves the depth resolution of the inversion results. Here, we apply this method to study the March 11 Tohoku earthquake. Three models produced during a protocol update procedure (Ji *et al*., 2004) will be presented here. The first one was online 6 hours after the rupture initiation and the third update was online on March 14, less than 72 hours after this catastrophic earthquake.

2. Multiple Double Couple (MDC) Analysis

Our investigation started with a Multiple Double Couples (MDC) analysis (Li and Ji, 2010). We selected 91 waveforms in vertical or transverse components of 51 teleseismic stations according to signal noise ratio (SNR) and azimuthal coverage. We removed the instrument responses, bandpass filtered from 166 s to 500 s, and aligned with PDE origin time (2011/03/11/05:46:23:70) reported by United States Geological Survey (USGS). Unlike the conventional

doi:10.5047/eps.2011.06.028

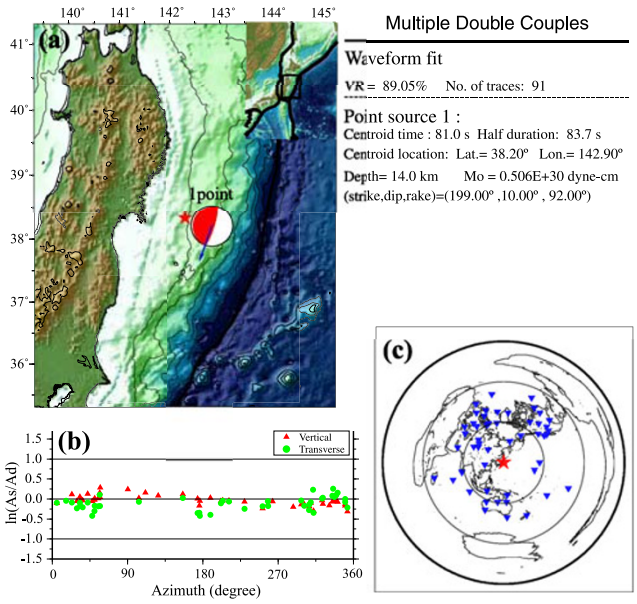

Fig. 1. Summary of the result of MDC analysis. The location of preferred point source is shown in (a), accompanying with USGS PDE location (red star) on the base of ETOPO2 topography. The red focal mechanism shows the preferred MDC solution and the blue arrow denotes the strike of the inferred low angle fault plane. The azimuthal variation of $\ln(A_s/A_d)$ is shown in (b) with red triangles and green circles for vertical and transverse components. The station locations are summarized in (c) as black triangles. The dashed contours denote 60° and 120° iso-distances. The values of inverted parameters are summarized in (b) as well as the average variance reduction (VR) and number of traces.

moment tensor inversion methods (e.g., Dziewonski and Woodhouse, 1983), our method, which aims to resolve focal mechanism change during the co-seismic rupture of large earthquakes, approaches an earthquake source as multiple double-couples. By matching the long period seismic waveforms within the first hour, we simultaneously invert for the centroid location (latitude, longitude, depth), centroid time, strike, dip, rake, and scalar moment of every point source. The half duration is fixed to be $2.26 \times 10^{-6} M_0^{1/3}$, where M_0 is the scalar moment in N m (Ekström *et al.*, 2005). The total number of free parameters is then $8N$, where N is the number of point sources. During the inversion, we gradually increase N until the F-test suggests that the consequent improvement in waveform fits is no long significant.

In spite of its large magnitude, we surprisingly found that a single double couple is sufficient to match the long period radiation of March 11$^{\text{th}}$ event. The corresponding variance reduction is 89%. Figure 1 shows the focal mechanism of this solution. Its low angle nodal plane has a strike of 199°, a dip angle of 10°, and a slip angle of 92°. The total seismic moment is 5.06×10^{22} N m, yielding a moment magnitude of 9.07. To illustrate the quality of corresponding waveform match, Fig. 1(b) compares the ratio of peak synthetic amplitudes (A_s) and observed amplitudes (A_d) by calculating $\ln(A_s/A_d)$. The model explains the data very well. The average value of $\ln(A_s/A_d)$ is -0.077 and the 2σ standard deviation is 0.30, suggesting that 95% of peak amplitude ratios (A_s/A_d) fall between 0.69 and 1.25. There is no obvious azimuthal dependent misfit pattern, so the source should be compact.

The fault dip and seismic moment are in remarkable agreement with the GCMT solution (`http://www.globalcmt.org`) that was available hours later. As the inverted centroid location (38.20°N, 142.90°E) is less than 100 km away from the trench axis (Fig. 1), the small dip angle of 10° is consistent with the plate interface revealed during a wide-angle reflection and refraction profile across the source region (Miura *et al.*, 2005). They reported that the dip angle of the subducted interface between 0 to 150 km from the trench axis changes from 5° to 12° (Miura *et al.*, 2005). Needless to say, to be able to quickly obtain a reliable focal mechanism is the most important *a priori* condition for a successful finite fault inversion.

3. Finite Fault Inversions

When the focal mechanism of the mainshock was available, we used teleseismic body and surface waves to constrain the spatiotemporal evolution of fault rupture. We have adopted the 3-phase procedure suggested by Ji *et al.* (2004). Phase I represents the fast solution that is constrained right after the event. Its fault plane is defined by the PDE location and the MDC/GCMT solution. And there is no correction to the arrival times. Phase II denotes the solution after refining fault geometry using the hypocenter constrained by local network and the information obtained from previous studies. Phase III denotes the further update after correcting the arrival times of *P* and *SH* waves using a well studied nearby fore/aftershock. In this section, we will first review the "*a priori*" conditions of each phase and then discuss the results of three phases together. The comparisons of observed and synthetic waveforms of following three models could be found in website (`http://www.geol.ucsb.edu/faculty/ji/big_earthquakes/2011/03/0311/Honshu_main.html`).

3.1 Model phase I

We defined a rectangular fault plane using the low angle nodal plane of the MDC solution and USGS PDE location (38.322°N and 142.369°E, depth = 24 km). The strike of fault plane has been slightly modified to 198° to match the orientation of the Japan trench axis. We considered a large planar fault with a dimension of 500 km (along strike) by 200 km (along dip). The source depth changes from 5 km to 39.5 km relative to sea level. This fault plane is further divided into 200 25 km by 20 km subfaults. The distance from the hypocenter to the tip of the fault plane is 110 km.

Our finite fault inverse method carries out the waveform inversion in the wavelet domain and applies a simulated annealing method to simultaneously invert slip amplitude, rake angle, rupture initiation time, and the shape of an asymmetric function for each subfault (Ji *et al.*, 2002, 2003). The total number of unknown parameters in this study is 1000. We let the slip amplitude vary from 0 to 40 m and rake angle change from 30° to 90°. We allowed the starting time and ending time of the asymmetric slip rate function (Ji *et al.*, 2003) to range from 1.6 to 16 sec. The value of rise time was therefore limited to 3.2 to 32 sec.

We used 27 teleseismic *P* and 13 *SH* waveforms, accompanying with 36 surface waves. The body waves were bandpass filtered from 2 s to 330 s. The surface waves were

Table 1. 1D velocity model interpolated from CRUST2.0.

V_p (km/s)	V_s (km/s)	Density (10^3 kg/m^3)	Thickness (km)
1.5	0.0	1.0	2.2
2.1	1.0	2.1	1.0
6.0	3.4	2.7	7.0
6.6	3.7	2.9	7.0
7.2	4.0	3.1	7.0
8.08	4.47	3.38	Half-space

*The last row is inferred from PREM model. The first layer was not used when forward calculating static displacement.

bandpass filtered from 166 s to 333 s. We aligned the body waves by the *P* and *SH* wave first arrivals predicted using the PDE hypocenter and IASPI91 travel-time table (Kennett and Engdahl, 1991) and then adjusted them slightly using the result of a preliminary inversion. During the inversion, we weighted teleseismic *SH* waves one half of *P* waves since the *SH* waves usually suffer large uncertainties of arrival times and low signal noise ratios. We double weighted surface waves relative to *P* waves, since Green's functions of long-period surface waves are much more reliable than body waves.

A 1D layered structure (Table 1) interpolated from the global CRUST2.0 (Bassin *et al.*, 2000) is used to approximate the earth structure in the source region. This model has a 2.2 km water layer, which might affect the response of fault slip in first 40–50 km away from the trench. The synthetic seismograms of body waves and long period surface waves were calculated using first motion approximation (Langston and Helmberger, 1975) and the normal mode superposition algorithm (e.g., Dahlen and Tromp, 1998), respectively. The dimension of subfault is too big to be treated as a single point source. We have further sampled every subfault with 195 uniformly distributed point sources to take into account the finiteness of individual subfaults (Ji *et al.*, 2002).

We use about 8700 wavelet coefficients extracted from the data to constrain 1000 source parameters. Because many of these coefficients are correlated, we still need stabilize the inversions by applying the derivative minimization smooth constraint of fault slip (Ji *et al.*, 2002), as well as a temporal constraint. The latter aims to compress the irresolvable roughness of rupture front, which is not well constrained because of the intrinsic trade-off between rupture initiation time and starting time (Ji *et al.*, 2003). Note that we could represent the rupture initiation time $t(x, y)$ at location (x, y) as the summation of a constant rupture field and a perturbation

$$t(x, y) = \frac{d(x_0, y_0; x, y)}{\overline{v}} + \delta t(x, y) \tag{1}$$

Here, $d(x_0, y_0; x, y)$ represents its on-fault distance to the hypocenter (x_0, y_0) and $\overline{v}$ is the rupture velocity averaging over the entire fault. Then we could compress irresolvable roughness of rupture fronts by minimizing $\nabla^2(\delta t(x, y))$. During the inversion, we also let $t(x, y)$ satisfy the following two conditions to further limit the model space,

$$\frac{d(x_0, y_0; x, y)}{v_{\max}} < t(x, y) < \frac{d(x_0, y_0; x, y)}{v_{\min}} \tag{2}$$

$$-T_P^{\max} < \delta t(x, y) < T_P^{\max}$$

The default value of $\overline{v}$ is 2.5 km/s and that of $v_{\min}$ is 1.25 km/s, both of which are subsequently updated using the result of the first preliminary inversion. For the following three models, we use a $\overline{v}$ of 1.5 km/s. $v_{\min}$ and $v_{\max}$ are 0.25 km/s and 3.5 km/s respectively in this study. $T_P^{\max}$ is 100 s. Finally, benefited by using long period surface waves, there is no need to constrain total scalar moment. We hereafter referred the inverted model "Model I". We show the map view of its inverted slip distribution in Fig. 2(a), and depict its moment rate function in Fig. 2(d). The total seismic moment is 5.6×10^{22} N m.

3.2 Model phase II

We then made many adjustments to the "*a priori*" conditions used in Model I. First, we used the local JMA location (38.106°N, 142.860°E, at depth of 24 km) as the rupture initiation, which is 50 km southeast of the PDE epicenter. The JMA origin time is 5.6 s earlier than the PDE origin time. These large discrepancies are likely due to the weak initiation rupture of the Tohoku earthquake, i.e., it could only be precisely detected at near-fault stations. We attempted to make the top of fault plane as close to trench axis as possible. The hypocenter depth was changed slightly to 23 km so that when the upper tip of fault plane has a depth of 7.5 km, which close to the sea floor depth at trench axis. The on-fault distance from the hypocenter to fault dip reduced from 110 km to 90 km. Second, we removed the southernmost column of subfaults because there was no significant slip in Model I. The total number of subfaults then decreases to 190. Third, we changed the maximum allowed slip from 40 m to 60 m because 13 subfaults of Model I have average slip over 39 m. Finally, we increased the amount of observations by using 27 *P*, 18 *SH* and 53 surface waves. We hereafter referred the inverted model "Model II". We show the map view of its inverted slip distribution in Fig. 2(b), and depict its moment rate function in Fig. 2(d). The total seismic moment of Model II is 5.84×10^{22} N m.

3.3 Model phase III

Regardless of the 9.1 magnitude, it is difficult to precisely pick the *P*, *SH* first arrivals at teleseismic stations. The inaccurate alignments result in a smeared slip distribution. The alignment could be significantly improved using a nearby large foreshock or aftershock (Ji *et al.*, 2004). Model phase III was constructed when we obtained a preliminary solution of the March 9$^{\text{th}}$ M_w 7.4 foreshock, which will be discussed in a separate effect. We notice that time shifts are up to 2 s for *P* waves, 6.8 s for *SH* waves, and 12 s for long period surface waves. We hereafter referred the inverted model "Model III". We show the map view of its inverted slip distribution in Fig. 2(c), and depict its moment rate function in Fig. 2(d). The total seismic moment is 5.75×10^{22} N m.

3.4 Results

Model I, II, and III have nearly the same seismic moment, changing negligibly from 5.6×10^{22} N m to 5.84×10^{22} N m.

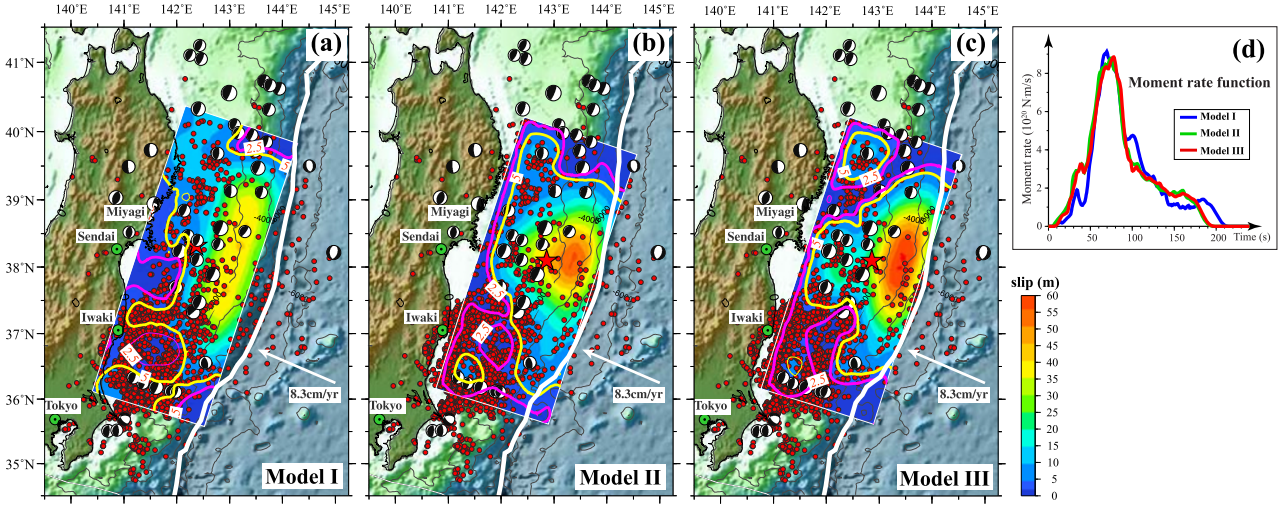

Fig. 2. Comparison of surface projections of slip model I, II, III by joint inverting teleseismic body and surface waves. Yellow line highlights the 5-m slip contour. Red star indicates the epicenter location and red dots are the aftershocks within first 6 days from JMA catalog. White arrow shows the Pacific plate motion relative to the North America plate (Demets *et al.*, 1994). (a) Model I. (b) Model II. (c) Model III. (d) Comparison of moment rate functions of UCSB Model I, II, and III.

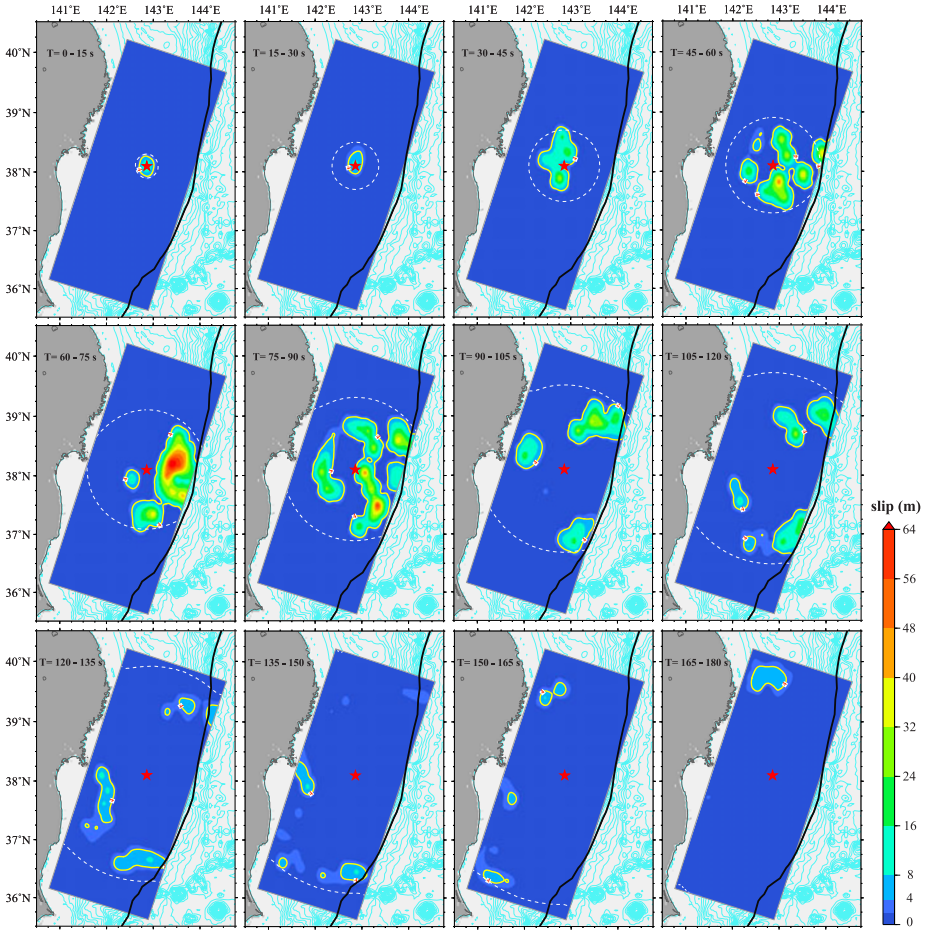

Fig. 3. Snapshots in a time interval of 15 s. The color shows the fault slip. The white dashed contour denotes the pseudo-rupture front for a rupture velocity of 1.5 km/s. 4-m yellow contours are used to indicate the majority slip during individual snapshots.

Their moment rate functions are also very similar, particularly the Model II and III (Fig. 2(d)). It can be seen that they all have a small peak at about 35 s, a burst of energy release from 45 s to about 100 s, and a long tail extending to over 150 s (Fig. 2(d)).

All of these models were dominated by a large asperity whose majority slip occurred between the hypocenter and the trench axis, where about 50–60% of total seismic moment occurred. However, the details of inverted slip distributions are affected by the changes we made. In Model I,

the aforementioned asperity has a rectangular shape, which is 325 km along strike (roughly from 36.5° to 39.5°) and 100 km along the down dip direction. The peak slip is 40 m. There is significant slip at northwest corner of the fault plane. In Model II, the big asperity shrinks along strike direction and the area also extends more to the downdip direction, west of the epicenter in a map view. The asperity then has a triangular shape with a peak slip of 56 m. The slip at the northwest corner significantly decreases in compared with that in Model I. We shall point out that the difference in peak slip is mainly caused by the limitation of maximum slip. A test with exactly the same "*a priori*" condition as Phase I except a maximum allowed slip of 60 m was preformed when we prepare this article, the inverted solution apparently fell between the Model I and Model II, with more slip concentrates right above the hypocenter and a peak slip of 58 m. Model III is very similar to Model II but apparently has more details. The triangular-shaped asperity was separated into two patches. We hereafter refer the patches above and below the hypocenter as "near trench asperity" (NTA) and "mantle asperity" (MA), respectively. Their peak slips are 60 m and 24 m respectively. The slip at the northwest corner further decreases in compared with Model II.

After comparing these three models, we conclude that the seismic moment and moment rate functionare well constrained. Although the shape of the major asperity is affected by the "*a priori*" information of fault model, the peak slip over 50 m near the trench axis is required by the data. In contrast, the slip patch at northwest corner might not be reliable.

The NTA was also captured by several other finite fault studies (e.g., Hayes, 2011; Lay *et al.*, 2011). But the 50–60 m peak slips of our solutions initially astonished the seismological community because it was a factor of two larger than other earlier solutions posted online. We shall point out that this is not a result of using a low rigidity model. The rigidity model we used is calculated using the 1D model in Table 1. In Model III, the accumulated seismic moment within the top 80 km is 3.3×10^{22} N m. Then even we uniformly distribute the slip in a rectangular area of 300 km by 80 km, the average slip is still 42 m, only 1/3 smaller. We believe our result would hold unless there are large errors associating with following two "*a priori*" conditions 1) MDC (and GCMT) fault dip 2) JMA hypocenter location. The differences in these two conditions might explain the differences in peak slips between our models and the USGS solutions (Hayes, 2011), which were constrained using the same software. Note that after aligning the data, the finite-fault inversion is analogous to a relative earthquake location problem. That the NTA is located in the east of the hypocenter is one of the most robust results. As the trench location is fixed, the hypocenter location controls the maximum potential width of NTA, which changes from 90 km for using JMA epicenter to 130 km for using USGS epicenter. Our Model I was not seriously affected because the original PDE hypocenter depth was 24.4 km rather than 33 km and we didn't attempt to match the upper tip of the fault plane with the trench axis. Considering the curvature of plate interface (Miura *et al.*, 2005), we suspect that the peak slip of near trench asperity (NTA) is underestimated, while that of mantle asperity (MA) might be overestimated.

The large slip near trench is not common for great ($M_w > 8$) subduction earthquakes. However, the 2011 Tohoku earthquake should not be counted as the only example. Another recent case we have studied is the 2006 M_w 8.3 Kuril island earthquake. Our inversion yielded a peak slip of 9 m near the trench axis. (`http://www.geol.ucsb.edu/faculty/ji/big_earthquakes/2006/11/15/kuril.html`). The geological post-tsunami survey in 2007 revealed up to 20 m local tsunami runups (MacInnes *et al.*, 2009). This preliminary slip model is also remarkably similar to the result of Lay *et al.* (2009).

Figure 3 shows the snapshots of Model III in a time interval of 15 s, which reveals a complex rupture process. The rupture initiated at a depth 23 km, near the forarc Moho discontinuity (Miura *et al.*, 2005). The beginning portion of rupture, especially the first 5 s, is very weak. During the first 30 s, the rupture propagated in a speed apparently less than 1 km/s, illustrating by the lag of rupture front at 30 s (outlined by the 4-m contour of fault slip) relative to the 1.5 km/s pseudo-rupture front (dashed curve, Fig. 3). The apparent rupture propagation significantly speeded up from 30 s to 45 s, accompanying with larger slip rate. It produced the first peak in the moment rate function (Fig. 2(d)). However, the rupture so far was limited on the subfaults with centroid depths same or deeper than the hypocenter, i.e., the top portion of MA. The failure of NTA, which on fault locates right above the hypocenter, didn't happen until at about 45 s. But as the rupture of NTA indeed initiated, it was explosive. The majority rupture of this 80 km wide asperity was accomplished in about 45 s, essentially producing the second peak of the moment rate function (Fig. 2(d)). After 90 s, the rupture of NTA continuously propagated bilaterally for another 45 s before ceased at 36.5°N to the south and at 39.5°N to the north at about 135 s approximately.

The MA failed again at about 70 s and the rupture propagated in the downdip direction toward the Oshika Peninsula for another 25 s (Fig. 3). The inverted peak slip of this subevent was 24 m. At about 110 s, another subevent initiated at (37.5°N, 142.0°E) approximately and ruptured bilaterally in a time period of 50 s. This rupture ceased near the Oshika Peninsula to the north and at approximately 36.25°N to the south (Fig. 3).

4. Discussions and Conclusions

All results presented in this article were obtained within the first three days after this catastrophic earthquake. As this is the first study in which our finite fault results relied on our in-house MDC focal mechanism, it is of interest to compare our results with other observations and solutions either online soon after the earthquakes or published recently.

We had verified the Model III by forward predicting coseismic slip of 343 GPS stations distributed by Caltech-JPL ARIA project. The synthetic displacements were calculated using the velocity model in Table 1. This comparison is presented in (`http://www.geol.ucsb.edu/faculty/ji/big_earthquakes/2011/03/0311/`

Honshu_main.html). It can be seen that the Model III is capable of predicting not only the general pattern of both horizontal and vertical co-seismic displacement fields but also their peak amplitudes. The mismatch in horizontal directions of bigger vectors could be easily reconciled by slightly shifting the MA northward. The solutions heavily based on the inland GPS dataset tend to map the slip more close to the hypocenter and have a significant reduce in slip toward the trench (e.g., Simons *et al*., 2011), inconsistent with our solutions. However, direct measurement of seafloor deformation near the trench axis indicates the average seafloor displacement of 50 m within the 40 km west of the trench axis (JAMSTEC, http://www.jamstec.go.jp/j/about/press_release/20110428/), which supports our solutions. Lay *et al*. (2011) obtained a similar large slip near the trench axis using only the teleseismic body waves after appropriately assigning the kinematic constraints.

Our kinematic rupture history (Fig. 3) is consistent with Ide *et al*. (2011). The three subevents on the fault plane deeper than the hypocenter were correlated well with the results of preliminary back-projection analyses (e.g., Wang and Mori, 2011). However, the rupture of NTA, which is crucial for exciting tsunami, was missed in back-projection analyses. The ruptures of MA around 30–45 s and 70–95 s were consistent with the two groups of explosive high frequency seismic radiations observed by local strong motion stations (http://www.knet.bosai.go.jp/knet/topics/TohokuTaiheiyo_20110311/nied_kyoshin2e.pdf).

Our calculation indicated that the failure of NTA led to about 10 m uplift near the trench axis, which is then essentially the cause of catastrophic tsunami. Giving the plate convergence speed of 8.3 cm/yr, the recurrence interval of such kind of events would be much longer than 500 yr.

Acknowledgments. The digital seismograms used in our inversions were downloaded from the IRIS data center provided by global seismograph network (GSN) and other networks such as GEOSCOPE, GEOFON, New China Digital Seismograph Network, etc. The GPS coseismic displacements were provided by Caltech-JPL ARIA project. Figures were prepared with the GMT software (Generic Mapping Tools) written by Paul Wessel and Walter H. F. Smith. This work was supported by NSF grant EAR-0911769, USGS Award number G09AP00023, the Southern California Earthquake Center, which is funded by NSF Cooperative Agreement EAR-0106924 and USGS Cooperative Agreement 02HQAG0008. We thank editor and two anonymous reviewers for their constructive reviews of manuscript.

References

Ammon, C. J. *et al*., Rupture process of the 2004 Sumatra-Andaman earthquake, *Science*, **308**, 1133–1139, 2005.

Bassin, C., G. Laske, and G. Masters, The current limits of resolution for surface wave tomography in North America, *Eos Trans. AGU*, **81**, F897, 2000.

Beck, S. L. and L. J. Ruff, Rupture process of the great 1963 Kurile Islands earthquake sequence—Asperity interaction and multiple event rupture, *J. Geophys. Res*., **92**, 14123–14138, 1987.

Dahlen, F. A. and J. Tromp, *Theoretical Global Seismology*, Princeton University Press, New Jersey, 1998.

Demets, C., R. G. Gordon, D. F. Argus, and S. Stein, Effect of recent revisions to the geomagnetic reversal time-scale on estimates of current plate motions, *Geophys. Res. Lett*., **21**, 2191–2194, 1994.

Dziewonski, A. M. and J. H. Woodhouse, An experiment in systematic study of global seismicity—Centroid-moment tensor solutions for 201 moderate and large earthquakes of 1981, *J. Geophys. Res*., **88**, 3247–3271, 1983.

Ekström, G., A very broad-band inversion method for the recovery of earthquake source parameters, *Tectonophysics*, **166**, 73–100, 1989.

Ekström, G., A. M. Dziewonski, N. N. Maternovskaya, and M. Nettles, Global seismicity of 2003: centroid-moment-tensor solutions for 1087 earthquakes, *Phys. Earth Planet. Inter.*, **148**, 327–351, 2005.

Hayes, G. P., Rapid source characterization of the 2011 M_w 9.0 off the Pacific coast of Tohoku Earthquake, *Earth Planets Space*, **63**, this issue, 529–534, 2011.

Ide, S., A. Baltay, and G. Beroza, Shallow dynamic overshoot and energetic deep rupture in the 2011 Mw 9.0 Tohoku-oki earthquake, *Science*, doi:10.1126/science.1207020, 2011.

Ji, C., D. J. Wald, and D. V. Helmberger, Source description of the 1999 Hector Mine, California, earthquake, part I: Wavelet domain inversion theory and resolution analysis, *Bull. Seismol. Soc. Am*., **92**, 1192–1207, 2002.

Ji, C., D. V. Helmberger, D. J. Wald, and K. F. Ma, Slip history and dynamic implications of the 1999 Chi-Chi, Taiwan, earthquake, *J. Geophys. Res*., **108**, 2412, 2003.

Ji, C., D. V. Helmberger, and D. J. Wald, A teleseismic study of the 2002 Denali fault, Alaska, earthquake and implications for rapid strong-motion estimation, *Earthq. Spectra*, **20**, 617–637, 2004.

Kennett, B. L. N. and E. R. Engdahl, Traveltimes for global earthquake location and phase identification, *Geophys. J. Int*., **105**, 429–465, 1991.

Kikuchi, M. and Y. Fukao, Inversion of long-period P-waves from great earthquakes along subduction zones, *Tectonophysics*, **144**, 231–247, 1987.

Kikuchi, M. and H. Kanamori, Inversion of complex body waves—III, *Bull. Seismol. Soc. Am*., **81**, 2335–2350, 1991.

Langston, C. A. and D. V. Helmberger, Procedure for modeling shallow dislocation sources, *Geophys. J. R. Astron. Soc*., **42**, 117–130, 1975.

Lay, T., H. Kanamori, C. J. Ammon, A. R. Hutko, K. Furlong, and L. Rivera, The 2006-2007 Kuril Islands great earthquake sequence, *J. Geophys. Res*., **114**, B113208, 2009.

Lay, T., C. J. Ammon, H. Kanamori, L. Xue, and M. J. Kim, Possible large near-trench slip during the 2011 M_w 9.0 off the Pacific coast of Tohoku Earthquake, *Earth Planets Space*, **63**, this issue, 687–692, 2011.

Li, X. and C. Ji, Investigation of long-period characteristics of great earthquakes through multiple point source analysis, presented at *2010 Fall Meeting, AGU*, edited, pp. Abstract S43A-2045, San Francisco, Calif., 13–17 Dec, 2010.

MacInnes, B. T., J. Bourgeois, T. K. Pinegina, and E. A. Kravchunovskaya, Tsunami geomorphology: Erosion and deposition from the 15 November 2006 Kuril Island tsunami, *Geology*, **37**, 2009.

Mendoza, C., S. Hartzell, and T. Monfret, Wide-band analysis of the 3 March 1985 central Chile earthquake—Overall source process and rupture history, *Bull. Seismol. Soc. Am*., **84**, 269–283, 1994.

Miura, S., N. Takahashi, A. Nakanishi, T. Tsuru, S. Kodaira, and Y. Kaneda, Structural characteristics off Miyagi forearc region, the Japan Trench seismogenic zone, deduced from a wide-angle reflection and refraction study, *Tectonophysics*, **407**, 165–188, 2005.

Simons, M. *et al*., The 2011 magnitude 9.0 Tohoku-Oki Earthquake: Mosaicking the megathrust from seconds to centuries, *Science*, **332**, doi: 10.1126/science.1206731, 2011.

Wang, D. and J. Mori, Rupture process of the 2011 off the Pacific coast of Tohoku Earthquake (M_w 9.0) as imaged with back-projection of teleseismic *P*-waves, *Earth Planets Space*, **63**, this issue, 603–607, 2011.

G. Shao (e-mail: shao@umail.ucsb.edu), X. Li, C. Ji, and T. Maeda